International Astronautical Congress, Sydney, Australia, 29 Sep-3 Oct 2025.

IAC-25-D2-7-6-x96123

System-Level Optimization and Validation of a Small Suborbital Launch Vehicle with Rocket and Jet Propulsion

Shinhyung Kim[a]*, **Sunghun Jung**[b]

[a] *Department of Smart Vehicle System Engineering, Chosun University, 61452, Gwangju, Republic of Korea* E-mail: vipsh.kim@chosun.kr

[b] *Department of Aerospace Engineering, Chosun University, 61452, Gwangju, Korea Republic* E-mail: jungx148@chosun.ac.kr

* Corresponding author

Abstract

Reusable sub-orbital launch vehicles with rocket and jet propulsion enable low-cost microgravity research and low-cost high-altitude exploration, while also supporting rapid payload delivery. Maximizing fuel efficiency with reliable retro-propulsive landing remains difficult for such heterogeneous propulsion. This paper presents a system-level optimization and validation framework that leverages existing engines and employs an Nonlinear Model Predictive Control (NMPC)–Extended Kalman Filter (EKF) control architecture, together with Sequential Quadratic Programming (SQP) to co-tune engine number, fuel allocation, initial jet fuel quantity, and NMPC weights and constraints.

Verification uses simulations validated against experiments that bracket expected hardware behavior with an ideal model and a mismatch model including gimbal backlash and spring-damper effects. The NMPC employs a simplified, differentiable prediction model for 10 Hz operation, and the EKF accounts for actuator nonlinearities such as gimbal backlash and compliance.

We quantified fuel-efficiency improvement and simulated landing precision. With NMPC optimization and hardware improvements, the horizontal landing error was reduced by 72.1 %, and fuel consumption decreased by 7.36 % over a 60-s flight simulation These results indicate that the proposed system-level co-design maintains landing accuracy and computational margin while improving fuel efficiency through system-level optimization.

The simulations establish a high-fidelity baseline for forthcoming scaled launch tests, where predicted and measured fuel usage will be compared by remaining fuel mass at touchdown and by pre- and post-flight mass accounting, and the models will be refined accordingly.

Acronyms

CG	Center of Gravity
EKF	Extended Kalman Filter
FF	Feed-Forward
GNC	Guidance, Navigation, and Control
MPC	Model Predictive Control
NED	North-East-Down
NMPC	Nonlinear Model Predictive Control
PID	Proportional-Integral-Derivative
SQP	Sequential Quadratic Programming
TVC	Thrust Vector Control
UAV	Unmanned Aerial Vehicle
VTOL	Vertical Takeoff and Landing
VTVL	Vertical Takeoff Vertical Landing

1. Introduction

Reusable sub-orbital launch vehicles that combine rocket and jet propulsion enable low-cost microgravity research and low-cost high-altitude exploration while supporting rapid payload delivery [1]. For such heterogeneous propulsion systems, mission viability depends on achieving high fuel efficiency together with reliable Vertical Takeoff Vertical Landing (VTVL) under tight state and input constraints, which recent reusable-launcher guidance and Guidance, Navigation, and Control (GNC) studies continue to emphasize [2, 3].

In this work the rocket provides high thrust-to-weight and altitude independence for ascent sequence, whereas the air-breathing jet engines are exploited in the denseair regime for energy-efficient loitering, deceleration, and precision VTVL landing. Jets draw oxidizer from the atmosphere and offer fine throttle authority and smooth low-thrust modulation near touchdown, which reduces fuel consumption. The heterogeneous architecture therefore targets mission-level efficiency and controllability, at the expense of added dry mass, inertia changes, and aerodynamic drag from the jet installation. These trade-offs depend strongly on the number and placement of jets and on mass properties, which motivates the proposed system-level co-tuning of configuration variables and Model Predictive Control (MPC) parameters in this paper (extending our propulsion-focused analysis in [4]).

Constraint-aware control based on MPC directly handles multivariable dynamics and constraints, but real-time operation at onboard rates and robustness under model mismatch remain central challenges [2, 3, 5]. In practice, actuator nonlinearities such as gimbal backlash and friction can degrade estimation and tracking unless they are explicitly addressed in the design and verification workflow [6]. Related Vertical Takeoff and Landing (VTOL)/Unmanned Aerial Vehicle (UAV) studies corroborate these issues in aggressive or failure-prone regimes [7–11].

For powered descent and landing, a complementary line of work has advanced guidance and feedback formulations that balance optimality and implementability, including convex and neighboring-optimal approaches and disturbance-rejecting feedback [12–16]. While these methods inform trajectory shaping and constraint handling, integrating them with vehicle- and actuator-level effects is still nontrivial in small reusable systems.

Recent control co-design literature argues for treating plant configuration and controller parameters as coupled decision variables to recover performance and robustness without excessive conservatism [17–20]. This perspective is particularly relevant when propulsion architecture, mass properties, and actuator authority co-determine feasible landing envelopes.

Our earlier study analyzed propulsion-level and fuel-efficiency trade-offs for rocket-jet candidates using existing engines and highlighted configuration trends and constraints for practical design, while intentionally excluding attitude control from the optimization to avoid confounding effects [4]. That separation exposed a gap between propulsion optimization and closed-loop landing reliability.

To close this gap, the present paper adopts a system-level optimization and validation framework. The control layer uses a split-fidelity stack with NMPC based on a simplified differentiable prediction model for 10 Hz updates and an EKF whose process model accounts for actuator nonlinearities such as gimbal backlash and compliance. On top of this stack, SQP is used to co-tune engine number, fuel allocation, inertia surrogates, and MPC weights and constraints so that fuel-efficiency objectives, landing accuracy, and computational margin are balanced under realistic operating conditions. Verification follows a bracketing strategy with experimentally validated simulations for an ideal model and a mismatch model that includes backlash and spring-damper effects; a quaternion Proportional-Integral-Derivative (PID) with Feed-Forward (FF) is included as a verification-stage baseline.

In summary, this work contributes: (i) a system-level co-design formulation that couples configuration variables with MPC tuning while preserving real-time feasibility; (ii) a split-fidelity NMPC and EKF architecture that improves robustness to actuator-induced mismatch without embedding non-differentiable effects in the optimizer; and (iii) a verification workflow based on experimentally validated simulations that establishes a high-fidelity baseline for forthcoming scaled experiments.

2. Vehicle Model

This section defines the vehicle configuration used for modeling, control, and validation. The overall system is conceived as a two-stage architecture in which a rocket stage carries a jet-propelled UAV toward the stratosphere. In this paper we validate a scaled configuration that exercises booster stage jet-engine VTVL only; the rocket is shown for context but remains inactive in the reported simulations. Figure 1a depicts the full rocket-UAV system, and Figure 1b shows the experimental configuration used here.

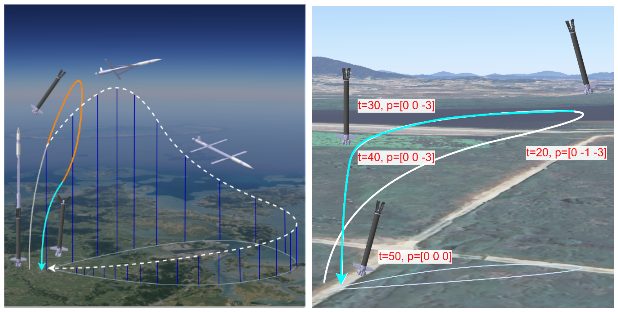

(a) (b)

Fig. 1: Flight profile of rocket and jet-propelled suborbital launch vehicle (a) and stage-1 configuration used in this validation (b).

2.1 Frames and geometry

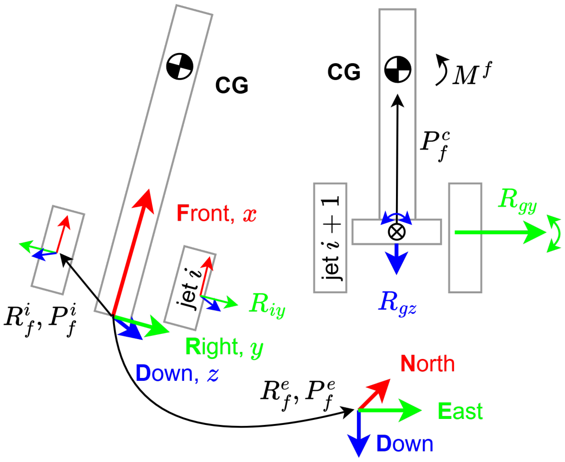

Fig. 2: Free body diagrams for the vehicle model.

The vehicle mounts i^{th} jet engines symmetrically on a gimbal frame and uses a single two-axis Thrust Vector Control (TVC) mount for the main rocket (inactive in this study). The body-fixed frame is indexed by f and the North-East-Down (NED) frame by e; frames and axes are defined in Figure 2. For jet i, the initial (zero-gimbal) attitude and position in the body frame are R_f^i and P_f^i.

2.2 State and Inputs

The state vector x consists of the quaternion q [$-$], angular velocity ω_f [rad/s], position $\vec{p}_e$ [m], velocity $\vec{v}_e$ [m/s], gimbal angle δ [rad], gimbal rate $\dot{\delta}$ [rad/s], throttle state ξ [$-$], and throttle rate $\dot{\xi}$ [$-$]. The input vector u consists of the commanded gimbal angles $\vec{\delta}_r$ [rad] and the commanded throttle ratio σ_u [$-$].

$$\begin{aligned} x &= \left[\, q^\top \;\; \omega_f^\top \;\; \vec{p}_e^\top \;\; \vec{v}_e^\top \;\; \delta^\top \;\; \dot{\delta}^\top \;\; \xi^\top \;\; \dot{\xi}^\top \,\right]^\top, \\ y &= \left[\, \omega_f^\top \;\; \vec{p}_e^\top \;\; \vec{v}_e^\top \,\right]^\top, \\ u &= \left[\, \vec{\delta}_r^\top \;\; \sigma_u^\top \,\right]^\top. \end{aligned} \tag{1}$$

2.3 Gimbal kinematics

The gimbal frame provides two rotational degrees of freedom about the body axes y_f (pitch) and z_f (yaw). Each jet engine is mounted to this gimbal frame, so that commanded gimbal deflections directly change the jet thrust orientation. An additional per-engine trim about the local y axis can also be included. The effective attitude of jet i is therefore

$$R_f^{i,\mathrm{eff}} \;=\; R_{\delta z}(\delta_z)\, R_{\delta y}(\delta_y)\, R_{iy}(\delta_x)\, R_f^i. \tag{2}$$

where $R_{\delta z}(\delta_z)$ and $R_{\delta y}(\delta_y)$ denote yaw and pitch rotations of the gimbal frame, $R_{iy}(\delta_x)$ denotes the local trim of jet i about its own y axis where δ_x assumed average δ_{iy}, and R_f^i is the fixed installation attitude of the engine.

2.4 Jet propulsion dynamics

Let T_i denote the commanded thrust for jet i in newtons. With a common per-jet maximum thrust $T_{\max}$, define

$$\sigma_{u,i} \;=\; \mathrm{sat}\left(\frac{T_i}{T_{\max}}\right) \in [0,1]. \tag{3}$$

Internal engine state ξ_i (with rate $\dot{\xi}_i$) represent the throttle delay as

$$\ddot{\xi}_i \;=\; k_c\left(\sigma_{u,i} - \sigma_i\right) \;-\; k_c\,\dot{\xi}_i. \tag{4}$$

The effective throttle ratio is

$$\sigma_i \;=\; \frac{e^{\,k_e\,\xi_i} - 1}{e^{\,k_e} - 1} \qquad (0 \le \sigma_i \le 1). \tag{5}$$

From eq. (5), the each jet thrust magnitude $T_{j,i}$ is

$$T_{j,i} \;=\; \sigma_i\, T_{\max}. \tag{6}$$

For simplicity in the present model, the jet system is represented by a single equivalent engine.

2.5 Actuation Mapping

In the general formulation, each jet i is modeled with a local FRD frame whose $+x$ axis is the thrust axis. Its effective attitude in the body-fixed frame is $R_f^{i,\mathrm{eff}}$ (built from the commanded gimbal angles and the fixed installation via eq. (2)). The commanded and effective throttle variables from the previous subsection produce the thrust magnitude $T_{j,i}$ [N], which acts along the jet's local $+x$ axis. In the simplified model used here, this reduces to a single equivalent engine with $T_{\max}$ denoting the total maximum thrust.

$$\vec{F}_{j,i}^{\,f} \;=\; R_f^{i,\mathrm{eff}} \begin{bmatrix} T_{j,i} \\ 0 \\ 0 \end{bmatrix}. \tag{7}$$

Forces and moments about the vehicle Center of Gravity (CG) are assembled by summation over all jets using the body-frame lever arms $\vec{r}_i^{\,f} = P_f^i - \vec{r}_{\mathrm{cg}}^{\,f}$ [m]:

$$\begin{aligned} \vec{F}_T^{\,f} &= \sum_{i=1}^{n_j} \vec{F}_{j,i}^{\,f}, \\ \vec{M}_T^{\,f} &= \sum_{i=1}^{n_j} \left(\vec{r}_i^{\,f} \times \vec{F}_{j,i}^{\,f}\right). \end{aligned} \tag{8}$$

When forces and moments must be expressed in NED, they are rotated by the body-to-NED matrix:

$$\vec{F}_T^{e} = R(q)\,\vec{F}_T^{f}, \tag{9}$$

where $R_f^e = R(q) \in \mathrm{SO}(3)$ is the body-to-NED rotation matrix by unit quaternion q in state x.

2.5.1 Gimbal frame dynamics.

The motion of the gimbal drive actuators is modeled as a spring-damper system, so that the commanded reference angles $\vec{\delta}_r = [\delta_{r,x}\ \delta_{r,y}\ \delta_{r,z}]^\top$ [rad] drive the actual gimbal angles $\vec{\delta}_y = [\delta_{y,x}\ \delta_{y,y}\ \delta_{y,z}]^\top$ [rad] through second-order servo models. Here K_p and K_d represent the effective stiffness and damping constants of the spring-damper model, J_{iyy} denotes the effective y-axis rotational inertia of the jet engine, and J_{gyy} denotes the y-axis rotational inertia of the gimbal assembly. The servo dynamics are written as

$$\begin{aligned}
\ddot{\delta}_x &= J_{iyy}^{-1}\big(K_{p,iy}(\delta_{r,x}-\delta_x) - K_{d,\mathrm{iy}}\dot{\delta}_x\big)\,,\\
\ddot{\delta}_y &= J_{\delta yy}^{-1}\Big(K_{p,\delta_y}(\delta_{r,y}-\delta_y) - K_{d,\delta_y}\dot{\delta}_y\Big)\,,\\
\ddot{\delta}_z &= J_{\delta yy}^{-1}\big(K_{p,\delta_z}(\delta_{r,z}-\delta_z) - K_{d,\delta_z}\dot{\delta}_z\big)\,.
\end{aligned} \tag{10}$$

2.6 Nonlinear Equations of Motion

Let $\vec{p}_e, \vec{v}_e \in \mathbb{R}^3$ be position/velocity in NED e. Mass m [kg]. The body inertia J_f [$\mathrm{kg}\cdot\mathrm{m}^2$] about the CG is constant and diagonal

$$J_f = \begin{bmatrix} J_{xx} & 0 & 0\\ 0 & J_{yy} & 0\\ 0 & 0 & J_{zz}\end{bmatrix}. \tag{11}$$

Forces and moments map $f \to e$ as

$$\vec{F}^{e} = R(q)\,\vec{F}_T^{f}, \qquad \vec{M}^{e} = R(q)\,\vec{M}_T^{f}, \tag{12}$$

Gravity is applied in NED. The rigid-body model is

$$\dot{\vec{p}}_e = \vec{v}_e\,, \tag{13}$$

$$\dot{\vec{v}}_e = \vec{g}_e + m^{-1}\big(R(q)\,\vec{F}_T^{f}\big)\,, \tag{14}$$

$$\dot{q} = \tfrac{1}{2}\,\omega_q \circ q, \qquad \|q\| = 1\,, \tag{15}$$

$$\dot{\omega}_f = J_f^{-1}\vec{M}_T^{f}\,, \tag{16}$$

where $\vec{g}_e$ [m/s^2] is gravity acceleration vector in NED frame, $\omega_q = [\,0,\ \omega_{f,x},\ \omega_{f,y},\ \omega_{f,z}\,]^\top$ is the pure quaternion of the angular velocity vector $\omega_f = [\omega_{f,x}, \omega_{f,y}, \omega_{f,z}]^\top$, and $\circ$ denotes quaternion multiplication. Therefore the equations of motion in component form are

$$\begin{aligned}
&\dot{q} = \tfrac{1}{2}\,\omega_q \circ q, \quad \|q\| = 1\,,\\
&\dot{\omega}_f = J_f^{-1}\vec{M}_T^{f}\,,\\
&\dot{\vec{p}}_e = \vec{v}_e,\\
&\dot{\vec{v}}_e = \vec{g}_e + m^{-1}\big(R(q)\,\vec{F}_T^{f}\big),\\
&\ddot{\delta} \text{ from } eq.\ (10),\\
&\ddot{\xi} \text{ from } eq.\ (4).
\end{aligned} \tag{17}$$

3. Controller Design

The control architecture was implemented as a NMPC and EKF stack. The NMPC operated at a fixed sampling period of 0.1 s with a simplified, differentiable prediction model that retained rigid-body and gimbal dynamics while omitting actuator backlash and compliance. Constraints on gimbal deflection, gimbal rate, and throttle authority were directly enforced in the optimization. The stage cost adopted the standard quadratic NMPC formulation penalizing output tracking error and input increments, and the associated nonlinear program was solved at each control step using a sequential quadratic programming (SQP) method [21]. The horizons, weights, and constraints applied in this work are summarized in Table 1. All values were initially selected heuristically by monitoring closed-loop convergence and simulation performance. They served as practical starting points and were subsequently refined within the system-level optimization framework to ensure consistency with the overall vehicle design objectives.

State estimation was provided by an EKF at the same update rate, propagating attitude, angular velocity, position, and velocity states. The EKF process model accounted for actuator effects including gimbal backlash and thrust-vector compliance, while the measurement model incorporated sensor bias and noise identified from bench calibration. This split-fidelity design allowed the NMPC to remain computationally tractable while the EKF compensated for higher-fidelity actuator and sensor effects excluded from the prediction model.

4. Simulation Setup

The simulation environment was implemented in a block-diagram based framework using a variable-step `ode45` solver with relative tolerance tighter than 10^{-3}. To relax command discontinuities, all commanded inputs from the controller were filtered by a first-order low-pass filter with a cutoff frequency of 100 Hz before being ap-

Table 1: Initial tuning configuration of the NMPC.

Number of state x	21
Number of output y	9
Number of input u	4
Prediction horizon	8
Control horizon	[4,2]
Output weights	$y_{1:3}(\omega_f)$: [1, 1, 1]
	$y_{4:6}(\vec{p}_e)$: [3, 3, 2]
	$y_{7:9}(\vec{v}_e)$: [2, 2, 2]
Input weights	$u_{1:3}(\vec{\delta}_r)$: [0.1, 1, 1]
	$\dot{u}_{1:3}(\vec{\delta}_r)$: [5, 1, 1]
	$u_4(\sigma_u)$: [1]
	$\dot{u}_4(\sigma_u)$: [1]
Relaxation weight	50
Output constraints	$y_{1:3}(\omega_f)$: [±2, ±15, ±15] deg/s
	$y_6(p_{e,z})$: ≤ 0 m
	$y_{7:8}(v_{e,x}, v_{e,y})$: ±2 m/s
Input constraints	$u_{1:3}(\vec{\delta}_r)$: [±3, ±15, ±15] deg
	$u_4(\sigma_u)$: $0.5T_{\max} \leq \sigma_u \leq T_{\max}$ N

All angular values are shown in degrees for readability, while radians were used internally in the implementation.

plied to the plant.

The baseline dynamics follow the nonlinear rigid-body formulation in Section 2. For verification, however, the equations of motion were integrated in the Earth-Centered Earth-Fixed (ECEF) frame instead of the local NED frame. This introduced explicit inertial and Coriolis forces due to Earth rotation and required modeling gravity as a position-dependent field rather than as a constant NED acceleration.

The high-fidelity plant incorporated actuator and sensor nonidealities on the physical side. The throttle path included identified delay dynamics (k_c, k_e), gimbal actuators exhibited backlash and rate limits, servo reaction torques were transmitted to the rigid body during gimbal motion, sensor outputs reflected calibrated noise and bias, and compliance of the thrust-vector mount was modeled as a spring-damper element. These refinements yielded a plant closer to experimental behavior, while the simplified baseline model remained embedded in the NMPC prediction layer.

The overall structure of the high-fidelity plant and its interfaces with the control layer with gimbal actuator are illustrated in **??**.

The gimbal actuator was implemented with an additional spring-damper stage and a backlash operator between the motor input and the gimbal inertia. This structure reproduced the compliance and play observed in hardware tests. An EKF was included to maintain observability of unmeasured gimbal states; detailed EKF performance is not the focus here and the model simplification is confined to the MPC prediction layer.

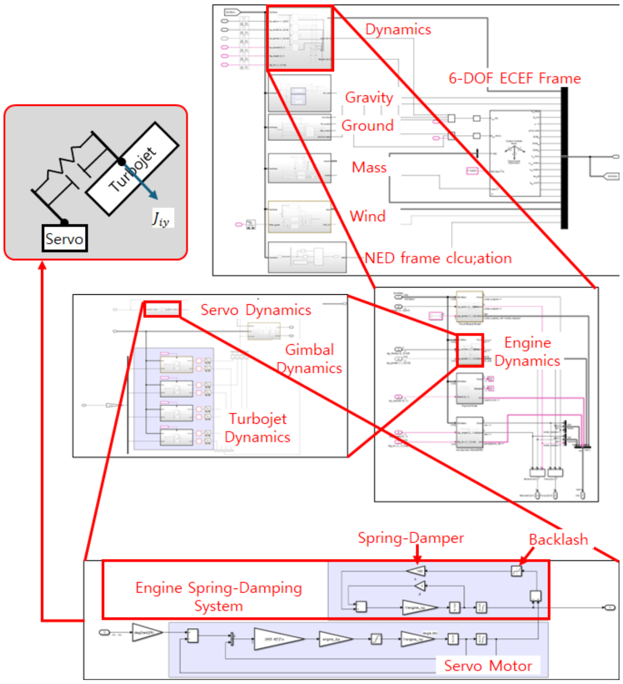

Fig. 3: Simulation block diagram with gimbal backlash and spring-damper effects.

Wind disturbances followed U.S. Military Specification MIL-F-8785C (Nov. 5, 1980) [22]: wind shear referenced to $1\,\mathrm{m/s}$ at $6\,\mathrm{m}$ altitude; continuous Dryden turbulence with reference wind $5\,\mathrm{m/s}$ at $6\,\mathrm{m}$ and a wingspan parameter of $1\,\mathrm{m}$; and a discrete 1-cosine gust starting at $20\,\mathrm{s}$ with lengths $120\,\mathrm{m}$, $120\,\mathrm{m}$ and $80\,\mathrm{m}$ and amplitudes $3.6\,\mathrm{m/s}$, $3.0\,\mathrm{m/s}$ and $3.0\,\mathrm{m/s}$, applied along the NED axes.

Initial conditions were set in the local NED frame with position $p = [0, 0, 0]$. The attitude was configured such that the body forward axis points upward in the NED frame, corresponding to a pitch rotation of $\pi/2$ rad. This is equivalently represented by the unit quaternion $q = [\cos(\pi/4),\ 0,\ \sin(\pi/4),\ 0]^\top$.

4.1 Parameter Identification

Model and estimation parameters used in the simulations were obtained as follows.

Thrust-throttle dynamics were fitted from prior propulsion tests, with k_c and k_e obtained through step-response

Table 2: Model parameters identified or assumed.

Parameter	Value	Notes
Number of engines n_j	2	Installed turbojets
Maximum thrust per engine [N]	26	Thrust bench data
Total maximum thrust $T_{\max}$ [N]	52	Equivalent engine model
k_c $[-]$	20	Thrust delay fit
k_e $[-]$	5	Thrust delay fit
J_{xx} [kg·m^2]	3.0765e-02	Torsional pendulum
$J_{yy} \approx J_{zz}$ [kg·m^2]	5.2328e-01	Torsional pendulum
J_{jyy} [kg·m^2]	6.3674e-04	Torsional pendulum (jet)
$J_{\delta yy}$ [kg·m^2]	1.4063e-02	Calculated from engine masses
Engine mass m_i [kg]	4.5000e-01	Measured
Dry mass m [kg]	4.1380e+00	Measured
CG P_f^c [m]	(4.0000e-01, 0, 0)	Balance arm and assumption (x, y, z)
P_f^1 [m]	(1.0000e-02, 8.8388e-02, 8.8388e-02)	Measured
P_f^2 [m]	(1.0000e-02, -8.8388e-02, -8.8388e-02)	Measured
R_f^1 [rad]	$(\pi/2,\ 0,\ 0)$	Installation Euler angles (roll, pitch, yaw)
R_f^2 [rad]	$(\pi/2,\ 0,\ 0)$	Installation Euler angles (roll, pitch, yaw)

delay characterization as reported in our previous study [4]. Aerodynamic coefficients such as lift slope were likewise extracted by CFD analysis in the same work for use in the simulation model.

Moments of inertia were identified using a bifilar torsional pendulum (see Figure 4), following [23]. Video recordings of the pendulum were processed using optical flow; the per-frame flow fields were spatially pooled into a single scalar motion-energy time series, and the dominant oscillation frequency was obtained by spectrum analysis (FFT peak), then converted to an angular frequency for identification. The roll inertia J_{xx} was measured directly, and the lateral and yaw inertias were found to be similar ($J_{yy} \approx J_{zz}$). The jet-engine inertia J_{jyy} was also obtained from the same torsional pendulum tests, while the gimbal inertia $J_{\delta yy}$ was calculated from engine masses as $\sum_i m_i r_i^2$. Basic mass properties such as engine mass and center of gravity were additionally obtained directly using scales and balance arms. Although no dedicated photographs were taken for these measurements, they provide the baseline values required for the simulation model. Table 2 summarizes all parameters used in the model, combining those identified experimentally with assumed values where measurements were not available.

4.2 *Scenarios*

All comparison runs used the same reference profile, wind conditions defined in §4, and fixed random seeds. Under this common environment, we contrasted three controller-plant configurations. To validate the NMPC design, we evaluated control performance with plant backlash removed, eliminating model-plant mismatch ("ideal model") in scenario I. We then enabled the measured backlash and compliance to assess robustness and the cost of model-plant mismatch, since the NMPC prediction model deliberately omits these nonidealities for tractability ("model-plant mismatch without optimized weights") in scenario II. Additionally, we considered an NMPC configuration whose weights were tuned via SQP while keeping the model-plant mismatch ("ideal model with optimized weights") in scenario III. Finally, we included a scenario with the ideal model and optimized weights to isolate the effect of weight tuning from that of model-plant mismatch. Although detailed optimization results are not presented here, this case provides a basis for the intended system-level

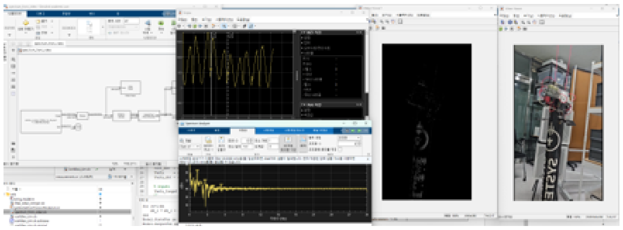

Fig. 4: Bifilar torsional pendulum experiment for inertia identification.

co-design, where hardware choices and NMPC weights are jointly optimized to minimize fuel, as outlined in the abstract and introduction.

The flight objectives common to all scenarios are listed in Table 3.

Table 3: Flight path reference positions.

Time t [s]	Position reference $\vec{p}_r = [x\ y\ z]$ [m]
0	$[0\ \ 0\ \ 0]$
1	$[0\ \ -1\ \ -3]$
20	$[0\ \ 0\ \ -3]$
$40 \le t \le 50$	$[0\ \ 0\ \ -3((50-t)/10)]$
50	$[0\ \ 0\ \ 0]$

The disturbance set applied to all configurations is as follows: baseline wind per MIL-F-8785C as defined in §4; additive sensor noise at levels typical of low-cost IMUs (no fixed bias imposed); measured TVC gimbal backlash applied as roll-axis $\delta_{iy} \in [-1°, +1°]$ and pitch/yaw $\delta_x, \delta_y \in [-2°, +2°]$; and center-of-gravity uncertainty bounded by $|\Delta x| \le 0.10$ m and $|\Delta y|, |\Delta z| \le 20$ mm. Each run uses the same initial conditions and random seeds across configurations.

5. Results and Discussion

We evaluate three outcomes—landing accuracy, fuel usage, and RMS error across the scenarios. Metrics are computed from the recorded output vector $y(t)$ and the simulation data. For consistency and readability, the graphs are presented in the ENU frame converted from the NED coordinates.

Landing accuracy uses the horizontal terminal error at landing position

$$e^{xy}_{\text{land}} = \left\|\vec{p}_{e,xy}(t_\infty) - \vec{p}_{r,xy}(t_\infty)\right\|_2, \tag{18}$$

where t_∞ is the terminal time.

Fuel is the cumulative consumption and its normalized fraction

$$\phi_{t_\infty} = m_{\text{fuel},t_\infty} - m_{\text{fuel},0}. \tag{19}$$

The RMS error e_{RMS} between the output trajectory $p(t)$ and the reference $p_r(t)$ is defined as

$$e_{\text{RMS}} = \sqrt{\frac{1}{t_\infty}\int_0^{t_\infty} \|\vec{p}(t) - \vec{p}_r(t)\|^2\, dt}, \tag{20}$$

where $p(t)$ is the position output in the NED frame, denoted as $y_{4:6}(t)$ in eq. (1). This value quantifies the controller's performance in tracking the reference trajectory.

Scenario I: ideal model without optimized weights The results serve to verify how well the model embedded in the MPC and the initial weight settings were applied. Despite unstable system dynamics, the MPC achieved stable attitude and position control. As time progressed, fuel consumption reduced the vehicle mass, yet the MPC decreased thrust accordingly and maintained proper flight control. However, since no further optimization had yet been performed, the convergence required a longer settling time.

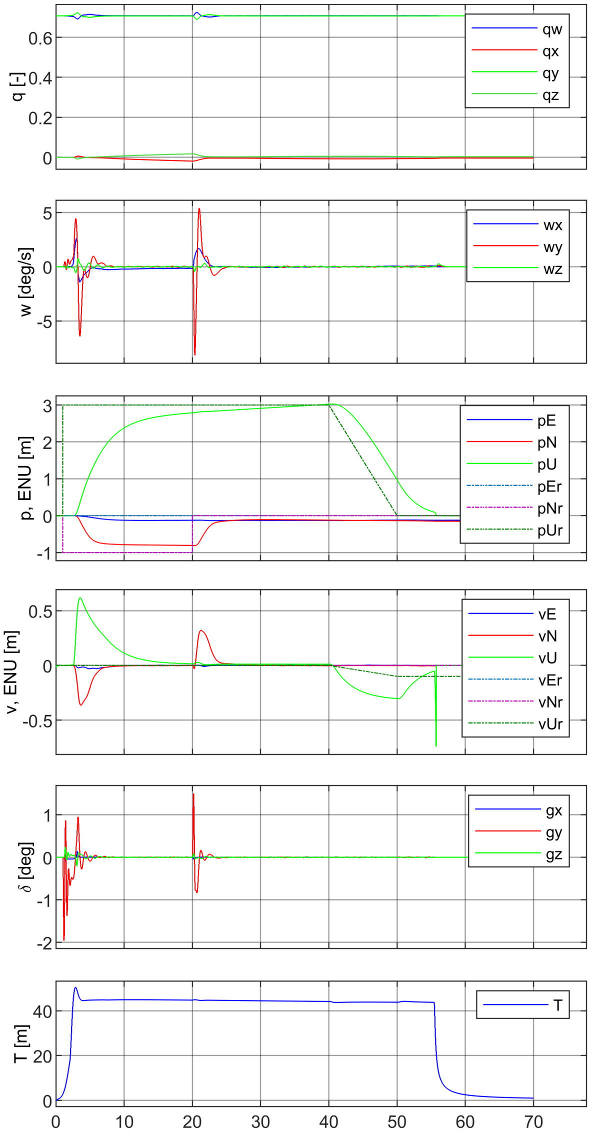

Fig. 5: Scenario I Measured outputs $y(t)$, gimbal angle $\delta(t)$ and Thrust $T(t)$.

Scenario II: model-plant mismatch without optimized weights When deadzone/hysteresis was applied using the measured gimbal-shaft play of 1° in d_x and 2° in d_y and d_z, the controller became unstable.

By contrast, applying the same deadzone only in the EKF process model yielded effective control without materially affecting the MPC's real-time feasibility. Figure 6 shows the corresponding results.

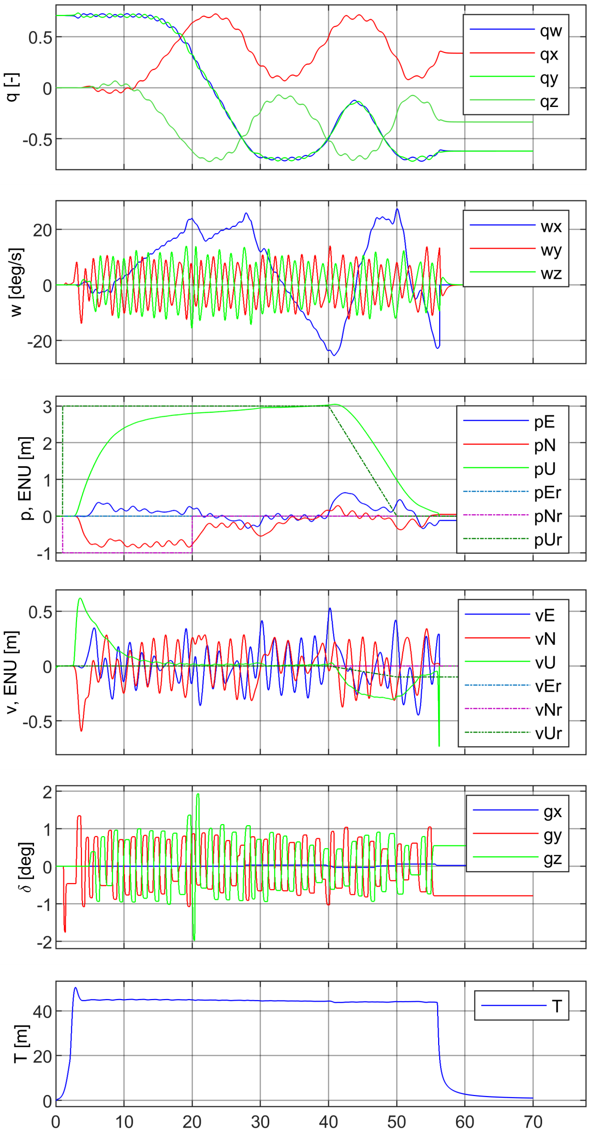

Fig. 6: Scenario II Measured outputs $y(t)$, gimbal angle $\delta(t)$ and Thrust $T(t)$.

Scenario III: model-plant mismatch with optimized weights The MPC weights were optimized to improve control stability and fuel efficiency, and the same flight trajectory as in Scenario II was simulated. Oscillations due to deadzone/hysteresis persisted, but overall control performance improved; in particular, the horizontal position error critical to landing was reduced after 40 s, and the peak gimbal deflection around 20 s was also lowered.

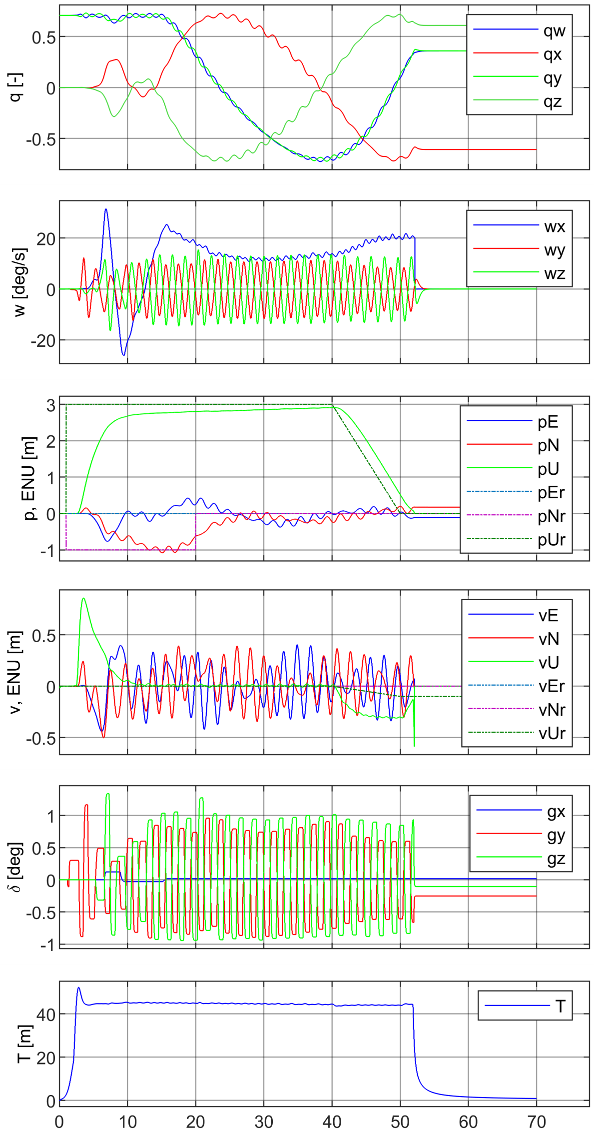

Fig. 7: Scenario III Measured outputs $y(t)$, gimbal angle $\delta(t)$ and Thrust $T(t)$.

Scenario IV: ideal model with optimized weights In this case, the plant backlash and compliance were removed as in Scenario I, while the NMPC weights were optimized via SQP to improve control stability and fuel efficiency. The simulation therefore isolates the effect of weight optimization under an ideal-model environment without hardware-induced mismatch. Compared to Scenario I, convergence to the commanded trajectory was faster and required smaller control excursions, while fuel consumption was slightly reduced.

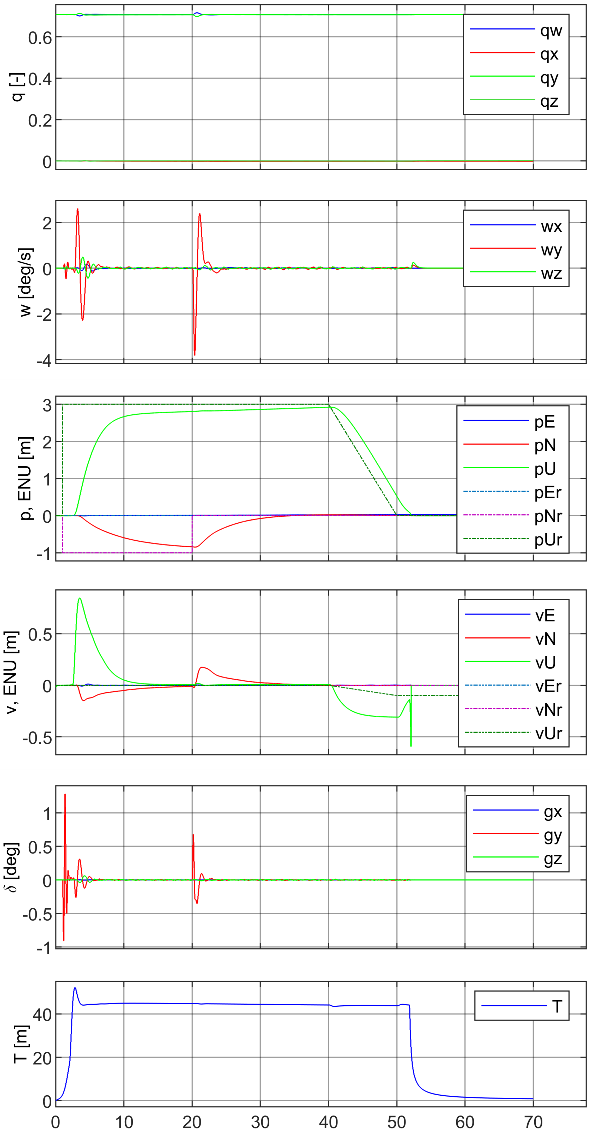

Fig. 8: Scenario IV Measured outputs $y(t)$, gimbal angle $\delta(t)$ and Thrust $T(t)$.

Table 4: Results summary.

Scenario	e^{xy}_{land} [m]	ϕ_{t_∞} [kg]	e_{RMS} [m]
I	1.9387e-01	1.7344e-01	1.1167e+00
II	1.2430e-01	1.7537e-01	9.8689e-01
III	2.0241e-01	1.6294e-01	9.0710e-01
IV	3.4680e-02	1.6245e-01	9.3932e-01

Table 4 summarizes the impact of model-plant mismatch (Scenario I vs. II), the performance gains from weight optimization under mismatch (Scenario II vs. III), and the maximum improvements achieved in this study (Scenario IV).

Quantitatively, Scenario IV achieved a 72.1% reduction in horizontal landing error and a 7.36% reduction in cumulative fuel usage over the 60 s flight compared to Scenario II; this reflects the *combined* effect of removing mismatch and tuning weights. For the weights-only effect under an ideal model, Scenario IV further improved upon Scenario I (e.g., e^{xy}_{land} decreased from $0.1939\,\text{m}$ to $0.0347\,\text{m}$, $\approx 82.1\%$; ϕ_{t_∞} from $0.1734\,\text{kg}$ to $0.1625\,\text{kg}$, $\approx 6.3\%$).

6. Conclusions

This work developed a system-level optimization and validation framework for reusable sub-orbital launch vehicles with heterogeneous propulsion. It integrates existing engines with an NMPC–EKF stack and uses SQP to co-tune engine count, fuel allocation, initial jet-fuel, and NMPC weights and constraints. Experiment-validated simulations bracketed behavior with an ideal model and a hardware-realistic mismatch model including measured gimbal backlash and spring–damper effects. Results show that model–plant mismatch degrades tracking, increases fuel use, and widens landing dispersion; SQP weight tuning recovers part of this loss while keeping 10 Hz real-time feasibility.

The proposed framework provides a reproducible, simulation-based optimization workflow and metrics that verify control feasibility of the simplified prediction model at 10 Hz for real-time use and assess alignment with hardware performance targets, thereby enabling rigorous preflight performance verification without flight tests.

Limitations are simulation-only validation and no full Pareto map over accuracy, fuel, and constraint margins. Future work will extend SQP under measured mismatch, broaden disturbance scenarios, and cross-validate on resource-constrained embedded computer and full-scale flight tests toward a 30 km mission profile.

Acknowledgements

This work was supported by the Korea Institute for Advancement of Technology (KIAT) grant funded by the Ministry of Trade, Industry and Energy (No. P0023691, Specialized Workforce Development Program for Space Materials, Parts, and Equipment) and by the Basic Science Research Program through the National Research Foundation of Korea (NRF) funded by the Ministry of Education (No. RS-2024-00414223).

References

[1] S.-S. Wei, M.-C. Li, A. Lai, T.-H. Chou, and J.-S. Wu, "A review of recent developments in hybrid rocket propulsion and its applications," p. 739, Sep. 2024.

[2] G. Zaragoza Prous, E. Grustan-Gutierrez, and L. Felicetti, "A decreasing horizon model predictive control for landing reusable launch vehicles," *Aerospace*, vol. 12, no. 2, p. 111, Jan. 2025.

[3] J. Guadagnini, P. Ghignoni, F. Spada, G. De Zaiacomo, and A. Botelho, "End-to-end gnc solution for reusable launch vehicles," *Aerospace*, vol. 12, no. 4, p. 339, Apr. 2025.

[4] S. Kim, A. Z. Woldeyohannis, G. T. Molla, M. Kim, E.-J. Park, and S. Jung, "Fuel efficiency analysis of the jet engine and solid-propellant based small reusable sub-orbital launch vehicle candidates," p. 790–797, 2024.

[5] J. Köhler, M. A. Müller, and F. Allgöwer, "Analysis and design of model predictive control frameworks for dynamic operation—an overview," p. 100929, 2024.

[6] Q. Zuo, B. Wang, J. Chen, and H. Dong, "Model predictive control of aero-mechanical actuators with consideration of gear backlash and friction compensation," p. 4021, Oct. 2024.

[7] J. Xia and Z. Zhou, "Model predictive control based on ilqr for tilt-propulsion uav," p. 688, Nov. 2022.

[8] F. Nan, S. Sun, P. Foehn, and D. Scaramuzza, "Nonlinear mpc for quadrotor fault-tolerant control," p. 5047–5054, Apr. 2022.

[9] L. Bauersfeld, L. Spannagl, G. Ducard, and C. Onder, "Mpc flight control for a tilt-rotor vtol aircraft," p. 2395–2409, Aug. 2021.

[10] M. A. K. Gomaa, O. De Silva, G. K. I. Mann, and R. G. Gosine, "Computationally efficient stability-based nonlinear model predictive control design for quadrotor aerial vehicles," p. 615–630, Mar. 2023.

[11] D. Wang, Q. Pan, Y. Shi, J. Hu, and C. Zhao, "Efficient nonlinear model predictive control for quadrotor trajectory tracking: Algorithms and experiment," p. 5057–5068, Oct. 2021.

[12] P. Lu and C. Davami, "Rethinking propellant-optimal powered descent guidance," p. 2016–2028, Oct. 2024.

[13] J. Wang, R. Zhang, and H. Li, "Endoatmospheric powered descent guidance," p. 112–121, Nov. 2024.

[14] X. CHEN, R. ZHANG, and H. LI, "Optimal feedback guidance with disturbance rejection for endoatmospheric powered descent," p. 103336, Dec. 2024.

[15] T. Reynolds, D. Malyuta, M. Mesbahi, B. Acikmese, and J. M. Carson, "A real-time algorithm for non-convex powered descent guidance," Jan. 2020.

[16] X. Chen, R. Zhang, W. Xue, and H. Li, "Robust neighboring optimal guidance for endoatmospheric powered descent under uncertain wind fields," p. 1491–1496, Aug. 2022.

[17] S. Azad and D. R. Herber, "An overview of uncertain control co-design formulations," Jul. 2023.

[18] G. W. Harris, P. He, and O. O. Abdelkhalik, "Control co-design optimization of spacecraft trajectory and system for interplanetary missions," p. 939–952, Jul. 2024.

[19] S. Kaneko and J. R. Martins, "Mdo formulations for simultaneous design and trajectory optimization," Jan. 2024.

[20] L. F. Fernandez, M. Bronz, T. Lefebvre, and N. Bartoli, "Simultaneous trajectory and design optimization of small vtol uavs with controllability considerations," Jul. 2024.

[21] J. B. Rawlings and D. Q. Mayne, *Model Predictive Control: Theory and Design*, 1st ed. Madison, WI, USA: Nob Hill Publishing, 2010.

[22] *Flying Qualities of Piloted Airplanes*, U.S. Department of Defense, Nov. 1980, november 5, 1980.

[23] M. R. Jardin and E. R. Mueller, "Optimized measurements of uav mass moment of inertia with a bifilar pendulum," *Journal of Aircraft*, vol. 46, no. 3, pp. 763–775, May-June 2009.